AGU
ADVANCING EARTH AND SPACE SCIENCE

Geophysical Research Letters®

The Devastating 2022 M6.2 Afghanistan Earthquake: Challenges, Processes, and Implications

S.-K. Kufner[1] ![ORCID], **L. Bie**[2] ![ORCID], **Y. Gao**[1] ![ORCID], **M. Lindner**[1] ![ORCID], **H. Waizy**[3] ![ORCID], **N. Kakar**[4] ![ORCID], and **A. Rietbrock**[1] ![ORCID]

[1]Geophysical Institute (GPI), Karlsruhe Institute of Technology, Karlsruhe, Germany, [2]School of Environmental Sciences, University of East Anglia, Norwich, UK, [3]Department of Geological Engineering and Exploration of Mines, Kabul Polytechnic University, Kabul, Afghanistan, [4]Global Geomonitoring and Gravity Field, German Research Center for GeoSciences (GFZ), Potsdam, Germany

Abstract On June 21st, a Mw6.2 earthquake struck the Afghan-Pakistan-border-region, situated within the India-Asia collision. Thousand thirty-nine deaths were reported, making the earthquake the deadliest of 2022. We investigate the event's rupture processes by combining seismological and geodetic observations, aiming to understand what made it that fatal. Our Interferometric Synthetic Aperture Radar-constrained slip-model and regional moment-tensor inversion, confirmed through field observations, reveal a sinistral rupture with maximum slip of 1.8 m at 5 km depth on a N20°E striking, sub-vertical fault. We suggest that not only external factors (event-time, building stock) but fault-specific factors made the event excessively destructive. Surface rupture was favored by the rock foliation, coinciding with the fault strike. The distribution of Peak-Ground-Velocity was governed by the sub-vertical fault. Maximum slip was large compared to other events globally and might have resulted in peak-frequencies coinciding with resonance-frequencies of the local buildings and demonstrates the devastating impact of moderate-size earthquakes.

Plain Language Summary The June 2022 devastating M6.2 Afghanistan earthquake has caused a high depth toll, making it the deadliest earthquake of 2022. This is notable and partly intriguing as the earthquake size is much smaller than other events that happened in 2022. Therefore, we combine a range of geophysical, geodetic and geological methods to understand how exactly the subsurface ruptured during the earthquake. We suggest that it was a combination of the local circumstances (the event time, as it hit at night time, and the building stock) and the geometry of the rupture surface together with the local geology that made this event particularly deadly. More generally, this study shows the excessive hazard and impact caused by moderate-size earthquakes.

1. Introduction

The 21 June 2022 Afghanistan earthquake occurred in a region dominated by the oblique collision of the Indian and Asian plates converging at ~34 mm/yr (Figure 1a; DeMets et al., 2010). Deformation is partitioned between ~26 mm/yr left-lateral strike-slip along the Chaman fault and the Kirtar-Sulaiman front fault that accommodates mostly thrust movement (~5–14 mm/yr N-S shortening; ~3–6 mm/yr W-E shortening; Bernard et al., 2000). Between these two structures, deformation is diffuse, expressed by multiple, partly cross-cutting faults. The 2022 event broke one of these secondary faults (Mohadjer et al., 2016; Ruleman et al., 2007) and featured a strike-slip rupture mechanism (Figure 1b), consistent with the broader tectonic context but not necessarily with the mapped faults. Magnitude estimates are between Mw 6.0 (USGS, 2022a) and 6.2 (GCMT, 2022).

The event was felt up to 500 km from the epicenter (USGS, 2022a). At least 1,039 people died and more than 2,900 were injured throughout eastern Afghanistan and western Pakistan, making it the deadliest earthquake of 2022 and in Afghanistan since 1998 (NOAA, 2023). Damage was strongest in Afghanistan, to the SW of the epicenter (Copernicus, 2022; European Union, 2022). The India-Asia collision zone is known to host destructive earthquakes, for example, the 2005 M7.6 Kashmir earthquake (Avouac et al., 2006). Yet, these events are mostly adjacent to the main plate boundary faults. Historic earthquakes within the region of the recent Afghanistan earthquake are rare and of smaller magnitude (Figure 1a).

In a global context, the Afghanistan earthquake was noticeably more destructive (factor of 2 regarding casualties) than events with a comparable rupture mechanism and magnitude (Figure 1c, Table S1 in Supporting Information S1). This observation poses the question of why the Afghanistan earthquake was so deadly. Was it due to the

Investigation: S.-K. Kufner, L. Bie, Y. Gao, M. Lindner, H. Waizy, N. Kakar, A. Rietbrock
Methodology: S.-K. Kufner, L. Bie, Y. Gao, M. Lindner, H. Waizy, N. Kakar, A. Rietbrock
Project Administration: S.-K. Kufner, L. Bie, A. Rietbrock
Resources: S.-K. Kufner, L. Bie, Y. Gao, M. Lindner, H. Waizy, A. Rietbrock
Software: L. Bie, Y. Gao, M. Lindner
Validation: S.-K. Kufner, L. Bie, Y. Gao, M. Lindner, H. Waizy, N. Kakar, A. Rietbrock
Visualization: S.-K. Kufner, L. Bie, Y. Gao, M. Lindner
Writing – original draft: S.-K. Kufner, L. Bie, Y. Gao, M. Lindner, H. Waizy, N. Kakar, A. Rietbrock
Writing – review & editing: S.-K. Kufner, L. Bie, Y. Gao, M. Lindner, H. Waizy, N. Kakar, A. Rietbrock

local time (1:24 a.m.) at which the event struck, the local building architecture, or is there any uniqueness in terms of the earthquake rupture property? A detailed investigation of the event is therefore critical to understanding its location and faulting characteristics - both relevant for seismic hazard mitigation and tectonic studies. Such an investigation typically uses regional seismic network recordings (e.g., Ross et al., 2018), which is less viable for this earthquake due to the sparsity of seismological data close to the epicenter (Figure 1d). To overcome this shortcoming, we combined geodesy, seismology and field observations, aiming to understand the earthquake's rupture characteristics and its devastating hazard.

2. Methods

2.1. Interferometric Synthetic Aperture Radar (InSAR) Modeling

Despite the sparsity of nearby seismic stations, the earthquake's epicentral area is well covered by Sentinel-1a Synthetic Aperture Radar (SAR) satellite data. We processed SAR images to obtain coherence maps (Figure 2a) and co-seismic interferograms (Figure S1 in Supporting Information S1).

To obtain earthquake source parameters, we first applied a joint deramp and atmospheric noise correction to the interferograms (Bie et al., 2014). We then performed a Bayesian inversion (Bagnardi & Hooper, 2018), assuming uniform slip on a rectangular fault buried in an elastic half-space (Table S2 and Figure S2 in Supporting Information S1). We next inverted for distributed slip on an extended fault-plane. We calculated a Green's function matrix using the Okada dislocation model (Okada, 1985) and applied a least squares inversion.

2.2. Regional Moment-Tensor (RMT) Inversion

We used the full waveforms of regional/local seismological data to calculate a RMT. Existing moment-tensors (MTs) are constrained mostly by teleseismic data. These solutions have similar strikes but vary in dip, rake, CLVD percentage, and location (Figure 1b and Table S2 in Supporting Information S1). To obtain a more accurate solution, we included several closer, non-publicly available seismic stations in the inversions (all Iranian stations, BTK and GLGT; see Figure 1d). To account for the complex geology in this region, waveform synthetics were computed in 3D velocity models (Gao et al., 2022; Simmons et al., 2021). We incorporated InSAR results by fixing the event's strike (N20°E) and epicenter (33.00°N, 69.47°E) to further reduce the uncertainty due to the sparsity of seismological data.

Our RMT inversion uses a Bayesian formulation via a uniform X-dimensional tree importance sampling of the parameterized geometric fault parameters and non-zero compensated linear vector dipole (CLVD) percentage (Tape & Tape, 2016). This allows us to include uncertainties from station delays or the origin time.

We inverted for solutions along a depth profile between 0 and 20 km in 1 km steps using bandpass filtered waveforms (0.02–0.035 Hz), windowed around the dominant transient signal (300 s). We sampled for the full range of dip (0°–90°), rake (−180° to +180°) and CLVD percentage (−100% to 100%). Time variations were permitted to account for station delay (<2 s) and origin time uncertainties (<5 s). This allowed us to compensate for model dependent delays from the teleseismic solutions in the origin time and uneven station delays due to different velocity models. Amplitude update between synthetics to observables yielded information about Mw.

2.3. Field Mapping

Field mapping was conducted approximately 1 month after the mainshock. Our field team traveled from the southernmost tip of the fault, as indicated from the InSAR study, toward NE, following the fault trace into the mountains, where the initial hypocenters from USGS (2022a) and Geofon (2022) had been located (Figure 1b). Field measurements were done using measuring tapes, GPS instruments, and handheld compasses. Mapping was conducted at three sites ~1.6, 1.9, and ~7.5 km off the InSAR-indicated fault trace (Figure 1b), where surface fractures were noticed by the local population. We also recorded building damage near the sites based on the Modified Mercalli Intensity (MMI) scale.

2.4. Peak-Ground-Velocity (PGV) Simulations

We calculated PGV based on our InSAR and RMT results considering the potential effects from 3D seismic velocity variations, through the 3D Radial Anisotropic Velocity model SPiRaL (Simmons et al., 2021), and high
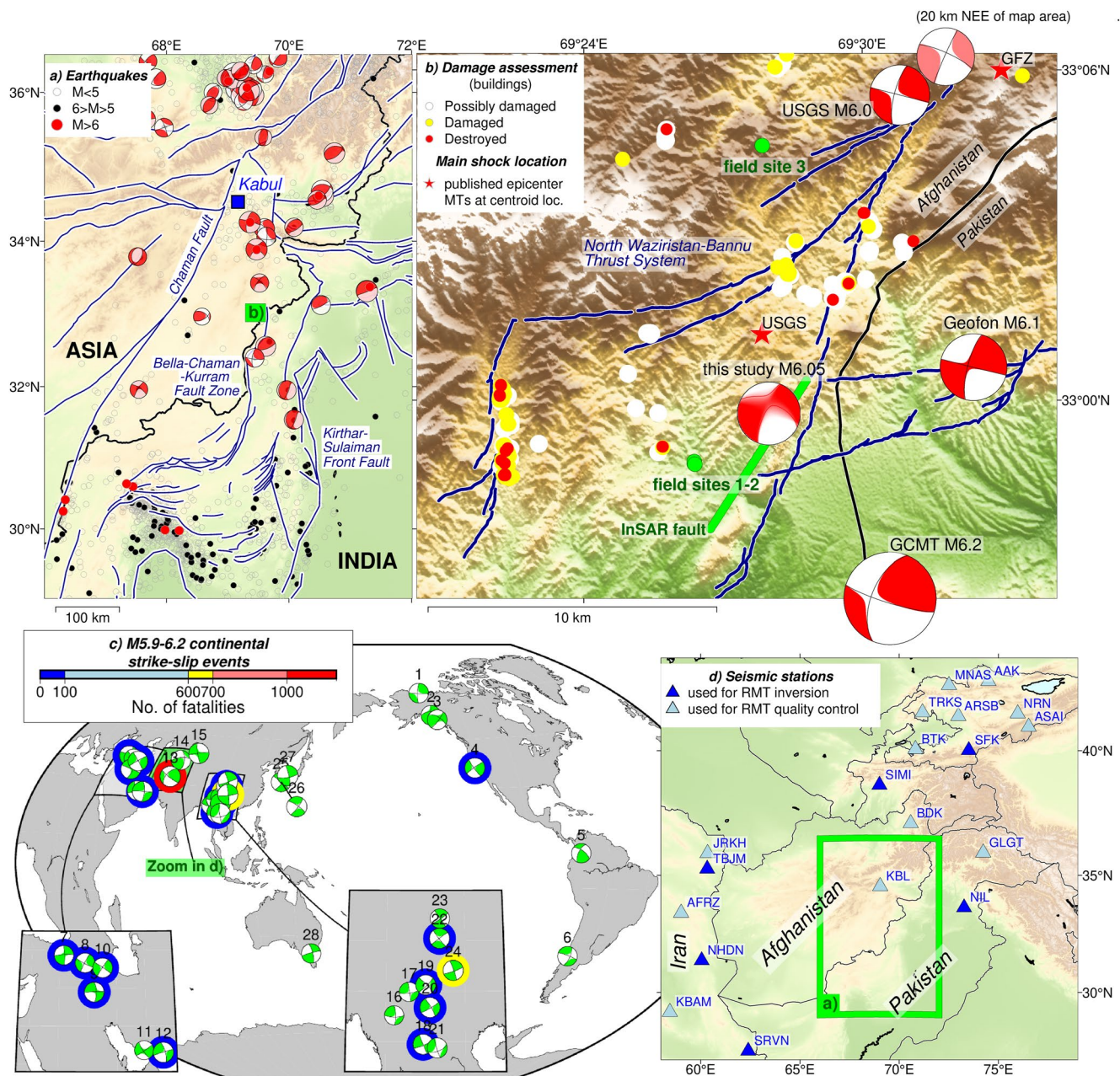
Figure 1. Tectonic background and global contextual earthquakes. (a) The Afghanistan earthquake in the India-Asia collision. Moment-tensors and earthquakes, shallower than 40 km since 1970 from CMT (Dziewonski et al., 1981; Ekström et al., 2012) and from USGS (USGS, 2022b). Faults (blue) from Mohadjer et al. (2016). Topography scale 0–6 km. Political boundaries in black. (b) Zoom into the study region. Faults (blue) from Ruleman et al. (2007), building damage assessment in selected regions from Copernicus (2022). See text for references to rupture mechanisms. Topography scale 1.8–2.8 km. (c) Strike-slip earthquakes with magnitude (Mw) 5.9 to 6.2 during the last 10 years (Dziewonski et al., 1981; Ekström et al., 2012). Only events in continental regimes are considered. Numbers refer to details in Figure 2d and Table S1 of Supporting Information S1. See Bayik (2021), Fathian et al. (2021), Gaudreau et al. (2019), Isik et al. (2021), Jiang et al. (2015), Jo et al. (2017), Kobayashi (2017), Liu et al. (2019), Niu et al. (2019), and Penney et al. (2015) for these earthquakes. Color corona refers to the number of fatalities, if available (NOAA, 2023). (d) Seismic stations either included in the Regional Moment-Tensor analysis or used for quality control. Topography scale and boundaries as in (a).

resolution topography (Hirt & Rexer, 2015; Pavlis et al., 2012), which both would have a major influence on simulated PGV (Wald & Allen, 2007). PGV measures the maximum surface ground velocity that occurred during shaking and can be used to estimate macroseismic intensity and structural damage (Bommer & Alarcon, 2006). We used PGV simulations to ground-truth our InSAR and RMT results and to understand the associated distribution of ground shaking. Results could be validated using waveforms of the KBL station (Figure 1d), through
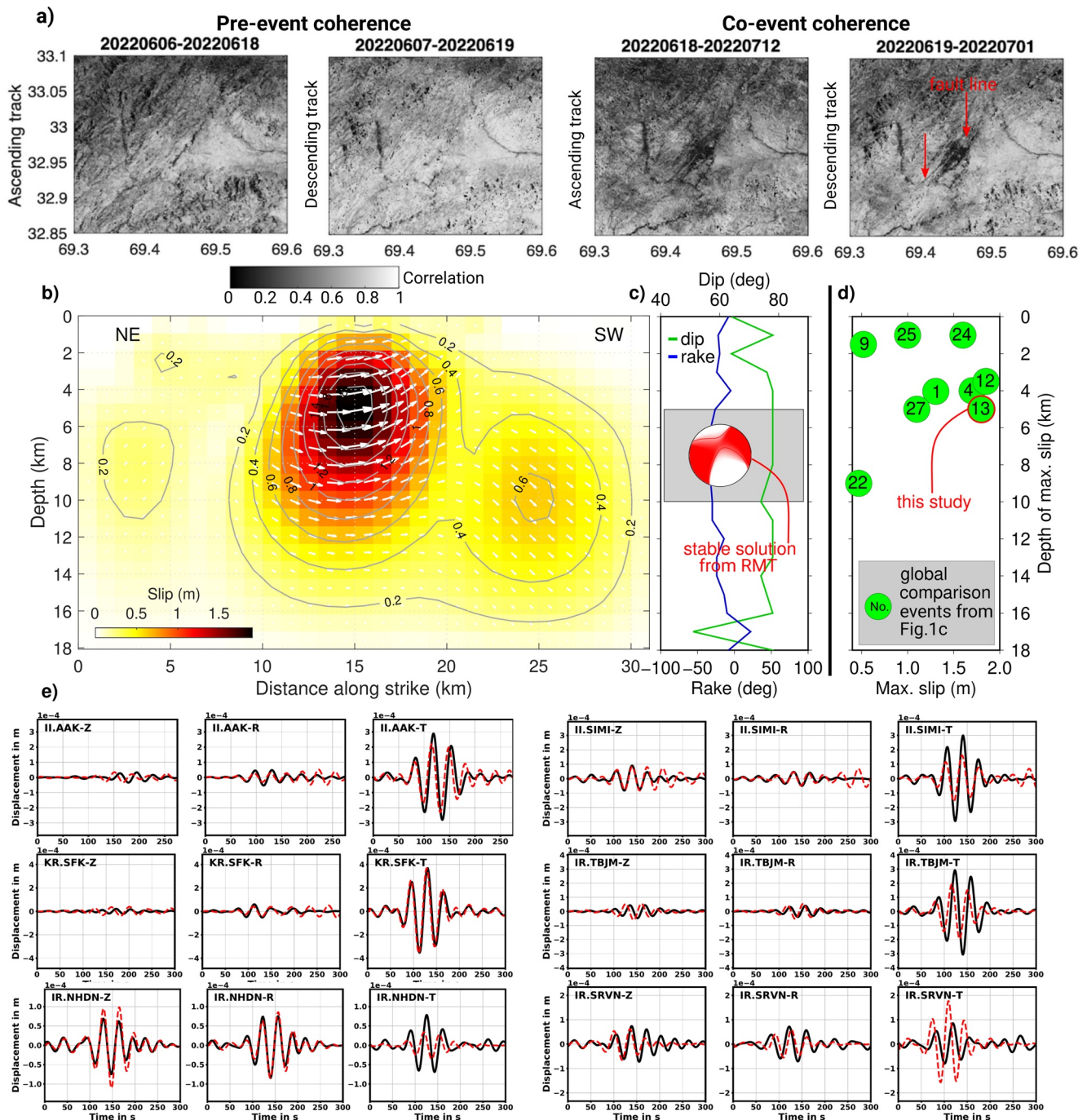
Figure 2. Compilation of InSAR and RMT results. (a) Coherence loss due to the earthquake defining the epicentral damage zone and likely the fault trace (highlighted by the red arrows). "Pre-event" shows the coherence of the interferograms before the event and "co-event" that spanning the event. (b) Distributed slip model from inversion of InSAR data. (c) Preferred RMT, plotted in red, with stable dip and rake values in the 5–10 km depth range. (d) Comparison of InSAR-constrained maximum slip and its depth between the Afghanistan earthquake and similar ones in terms of magnitude and rupture mechanism (number refer to those in Figure 1c and Table S1 in Supporting Information S1). (e) Comparison of observed (black) and predicted (red) waveforms for the preferred RMT solution (see Figure 1d for station locations).

empirical PGV-shakemaps based on "Did you Feel it"-reports from USGS (2022a), and through our MMI observations.

We used the Spectral Element Method (software Salvus; Afanasiev et al., 2019) on a $600 \times 600 \times 200$ km mesh to simulate high-frequency seismic wave propagation (up to 1 Hz) for 3,600 virtual stations and the station KBL,

which is closest to the epicenter (see simulation details in Text S2 of Supporting Information S1). Two scenarios were simulated. One with our point-source RMT solution and one with the finite-fault slip model (see result details in Figures S3 and S4 of Supporting Information S1).

For the point-source, we used 2.6 half duration of the source time function as the main pulse was around 5.2 s (USGS, 2022a). Since the centroid source depth from RMT allows for some flexibility, we simulated the synthetics for source depths of 7, 10, and 12 km and calculated the misfits of the Maximum-Amplitude-Envelope (MAE) between observed and synthetic of the velocity seismograms at KBL. For comparison, we also derived MAE at the KBL stations for the MTs from USGS (2022a), GCMT (2022), and Geofon (2022).

For the finite-fault simulation, we discretized the fault-plane from InSAR into 589 double-couple subevents (Figure S4 in Supporting Information S1). We used 2 km/s rupture speed (~80% shear-wave velocity at 1–4 km depth; Shearer, 2009), starting from the hypocenter of USGS (2022a). According to the frequency spectrum of the observed waveforms (Figure S5 in Supporting Information S1), we assumed a Gaussian rate source time function with 1 s half duration for the subevents. We perturbed the hypocenter depth from 2 to 12 km with 2 km intervals and compared the synthetics with the KBL velocity records.

3. Results and Interpretation

3.1. Earthquake Source Parameters From InSAR

The coherence change after an earthquake helps to identify fault damage zones (e.g., Yun et al., 2015). In our coherency maps, a dark linear trace is observed in the epicentral area (Figure 2a, right), indicating that the earthquake ruptured to the surface. Compared to the northern part of the fault, the central-southern part experienced more coherence loss, suggesting a wider fault damage zone and/or secondary features such as landslides.

The distributed slip model (Figure 2b) shows one main patch with a maximum 1.8 m of slip at ~5 km depth. This result for depth of maximum slip is comparable with other events globally, whereas the maximum slip is at the upper end (Figure 2d). Additional patches of slip with significantly smaller amplitude are found in the NE and SW parts of the fault-plane at slightly greater depths. These likely mark early afterslip following the mainshock.

3.2. Earthquake Source Parameters From RMT Inversion

Our RMT results support a dominant left-lateral strike-slip source (Figure 2c). Pinpointing an exact depth based on the variance reduction (VR) turned out to be difficult. This is due to the narrow frequency band at the lower end of the excited wavelength and due to the trade-off between station time shifts, origin time updates and event depth. Thus, we obtain a depth estimate of 5–10 km, where VR is 53% (Figure 2e and Figure S7 in Supporting Information S1), by comparing the variations in dip, rake, and CLVD (Figure 2c and Figure S6 in Supporting Information S1). The fault dip and rake are stable within this depth range and consistent with our InSAR model. For this depth range the fault dips constantly to the WNW (around 78°), with a fluctuating rake from −26° at 5 km to −38° at 7 km and −30° at 10 km (Figure 2c). The CLVD part decreases near linearly from 25% at 5 km depth to −12% at 10 km depth (Figure S6 in Supporting Information S1). The moment magnitude, dependent on the CLVD, is 6.05 ± 0.03. One possibility to explain the CLVD percentage could be two subevents, which can however not be constrained uniquely based on the available data (details in Section S1 and Figure S8–S10 of Supporting Information S1).

3.3. Field Observations and Building Damage

Our third set of results comes from field observations. At all visited sites, rocks are mostly shales and schist, covered with soil (Figures 1b and 3 and further details in Figures S11–S17 of Supporting Information S1). Only site 3 is covered with vegetation. Google-Earth imagery traces a ~N40°E-striking structural grain that we interpret to mark the strike of the rock foliation (Figure 3a).

At site 1, 1.9 km off the InSAR-derived fault trace, we observed one continuous ~46 m long, segmented rupture. The fractures (up to 40 cm fracture-normal offsets; up to 1.5 deep) strike ~N30°E and cut obliquely across the foliation. We consider them as a composite of secondary features, including syn- and antithetic Riedel shears with a tensional component and oblique-slip tension fractures, likely enhanced by down-slope movements (Figure 3b and Figure S13 in Supporting Information S1). Site 2 (Figures 3d and 3e and Figure S14 in Supporting Information S1) is closest to the fault line constrained by InSAR (1.6 km offset). We observe more, longer (up to 150 m),
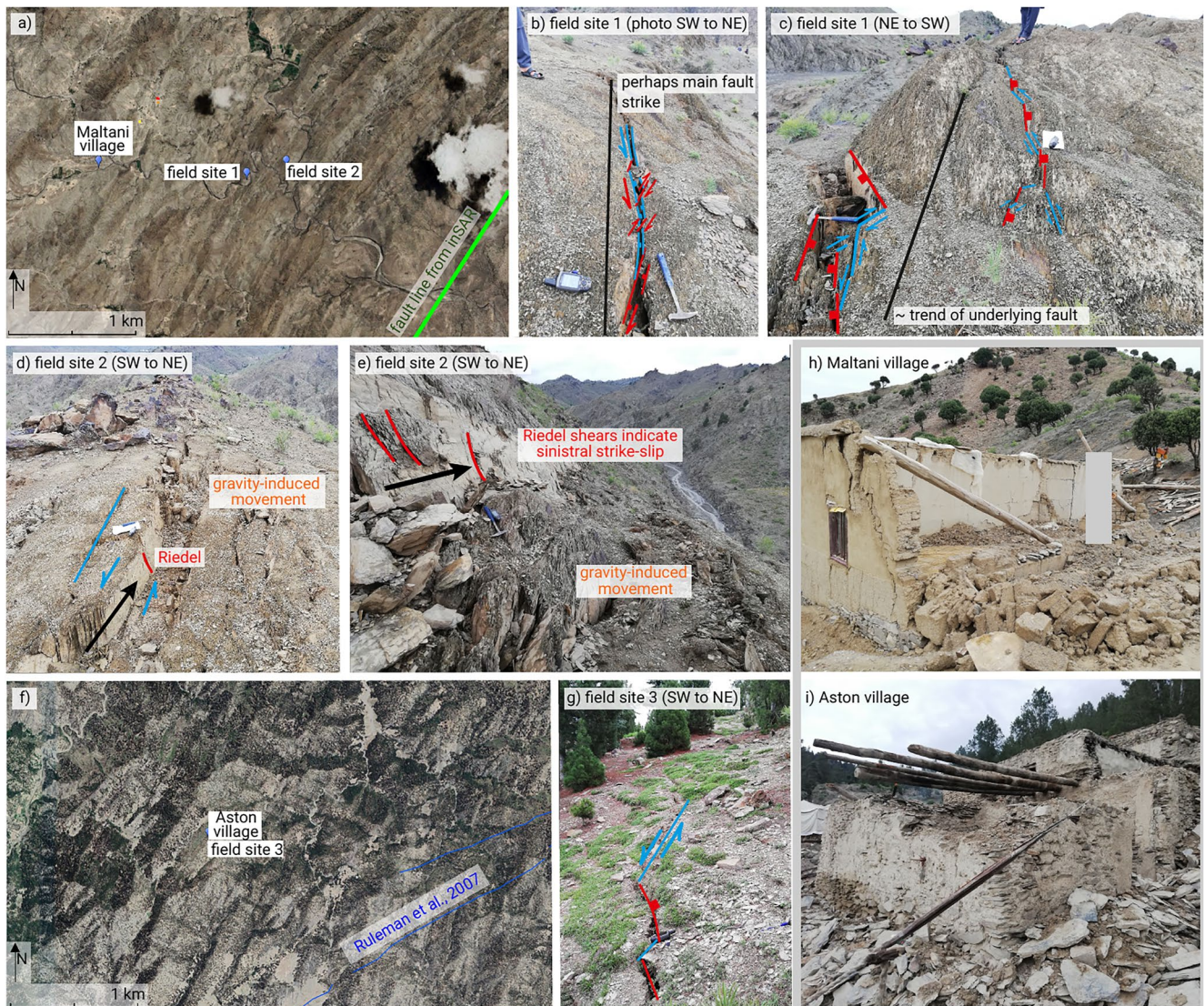
Figure 3. Geological field and building damage observations. (a) Close-up map of field sites 1 and 2. Background image from Google Earth Pro V7.3.4.8248 (2022). (b and c) Field pictures from field site 1. The slope faces east. (d and e) Field pictures from field site 2. (d) is at a mountain top. Panel (e) is along an east-facing mountain slope. (f) Close-up map of field sites 3. Background image from Google Earth Pro V7.3.4.8248 (2022). (g) Field pictures from field site 3, taken at a west-facing slope. (h and i) Destroyed houses near field sites 1 and 3.

and deeper (up to 3 m) fractures. The average ~N25°E strike of all features is similar to site 1 and nearly coincides with the strike of the InSAR-determined fault line. The striation on the fresh fault surfaces are subhorizontal and synthetic Riedel shears on subvertical fault surfaces manifest the sinistral slip-sense. We also observed gravitationally induced mass movements (up to 1 m vertical offset) along steep slopes (Figure 3e). Site 3 (Figures 3f and 3g and Figure S15 and S16 in Supporting Information S1) is farthest away from the fault trace (7.5 km offset). Fractures strike similar as those at sites 1 and 2 but their depths and offsets (4–11 cm) are smaller. We interpret these fractures as secondary features, mainly composed of synthetic Riedel shears and tensional fractures. In sum, the field survey showed a decreasing intensity of occurrence of co-seismic features from the site closest to the fault line, to the site farthest away. Most surface-rupture features in bedrock strike subparallel to the fault outlined by InSAR, although the field sites are located at differently oriented hillslopes. This suggests that these features are directly related to the earthquake.

As typical for this region, almost all houses are made from clay bricks, and most of the roofs have a wooden frame (Figures 3h and 3i and Figure S17 in Supporting Information S1). These constructions had been further weakened through a rainy period prior to the earthquake (World Meteorological Organization, 2022). In most houses,

roofs were destroyed due to their heavyweight and the brittle architecture of the walls. At all locations, villagers reported earthquake effects that indicate intensities between VIII and IX based on the MMI scale.

3.4. Ground Shaking Simulation (PGV)

We obtained 10 km centroid depth assuming a point-source and 4 km hypocentral depth for the finite-fault simulation (waveforms and MAE comparison in Figures S18–S20 of Supporting Information S1). The centroid depth for the point-source is consistent with solutions published by USGS (2022a) and Geofon (2022). However, our waveform fitting (Figures 4c and 4d) is significantly improved in comparison to the earlier published results (Figure S20 in Supporting Information S1), highlighting the quality of our RMT solution.

For the point-source, the far-field PGV (over 50 km epicentral distance) roughly agrees with results from the empirically derived USGS-shakemap (USGS, 2022a). In the near-field, PGV from USGS (2022a) is over 20 cm/s and up to 53 cm/s, higher than the maximum estimate from our single-point-source simulation (10 cm/s) (Figure 4a and Figure S21 in Supporting Information S1). By contrast, incorporating the finite slip model increased the near-field PGV within 10 km epicentral distance to ~47 cm/s (Figure 4b and Figure S21 in Supporting Information S1), consistent with the empirical predictions. Lastly, calculating the empirical MMI from the finite-fault PGV via scaling relationships (Worden et al., 2012) at our field sites resulted in intensity values between IX (sites 1 and 2) and VIII (site 3). This is comparable to the intensity values obtained in our field study. The discrepancy in the near-field between point-source and finite-fault simulations highlights the importance of including a finite-fault model when calculating near-field PGV. The effect is negligible in the far-field.

4. Discussion and Conclusions: Source Process and Implications

Our analysis reveals for the Mw6.2 Afghanistan earthquake a sinistral strike-slip mechanism with maximum slip of 1.8 m at 5 km depth on a sub-vertical, N20°E-striking fault. Both fault location and slip direction were independently confirmed through field observations. The RMT suggests a rake angle of $\sim-31°$ and a centroid depth between 5 and 10 km. We calculated PGV based on our analysis including 3D velocity models and high resolution topography and obtained a highly asymmetric pattern relative to the fault. Compared to teleseismic MTs, improved waveform fitting confirmed the reliability of our RMT solution despite the sparse seismological data coverage. The relatively small discrepancy between the centroid depth and depth of maximum slip from InSAR inversion may arise from the lack of seismic stations in the near-field and highlights the need to do complimentary inversions. However, it clearly shows that using modern techniques it is now feasible to determine reliable source parameters for hazard assessment even for cases where the data availability is challenging. Both InSAR and RMT results hint toward a complex rupture, including afterslip and possibly involving two subevents during the main rupture.

Aiming to understand what made the Afghanistan earthquake that fatal, we compared these faulting characteristics with other continental strike-slip events within the same magnitude range (Figure 1c and Table S1 in Supporting Information S1). Our summary covers a wide range of geographical locations, including deserts (e.g., event 11 in Iran) and highly populated regions (e.g., events 4, 24, and 25–27 in California-USA, China, and Japan). These earthquakes occurred in countries with distinctly different development status, which may affect the quality of the buildings and/or the implementation of seismic building codes (Ambraseys & Bilham, 2011). Many of these earthquakes hit at nighttime, as the Afghanistan event did. Nevertheless, the Afghanistan event caused by far (factor 2) the highest death toll. Searching for differences in the faulting characteristics, we compared events with available InSAR solutions (Figure 2d and Table S1 in Supporting Information S1) and found that the depth of peak-slip in these models varies between 1 and 9 km, with an average at 3.78 km. Maximum slip varies from 0.5 to 1.85 m (average: 1.25 m). Thus, the slip and the depth of the Afghanistan event was comparable to other similar magnitude events globally, but the peak-slip value was at the upper end. Maximum slip of the Afghanistan event is also larger than expected from global scaling relationships (see Figure S22 in Supporting Information S1 and Brengman et al. (2019) for details).

Based on this comparison and the faulting characteristics derived in this study, we suggest that it is a combination of different factors that made the Afghanistan event that deadly. First, the earthquake struck at night, which enhanced the fatal impact of this specific earthquake as most fatalities were caused by collapsing houses. Thus, the stone-mud architecture of most buildings, which were further weakened by rain, are likely the main factors
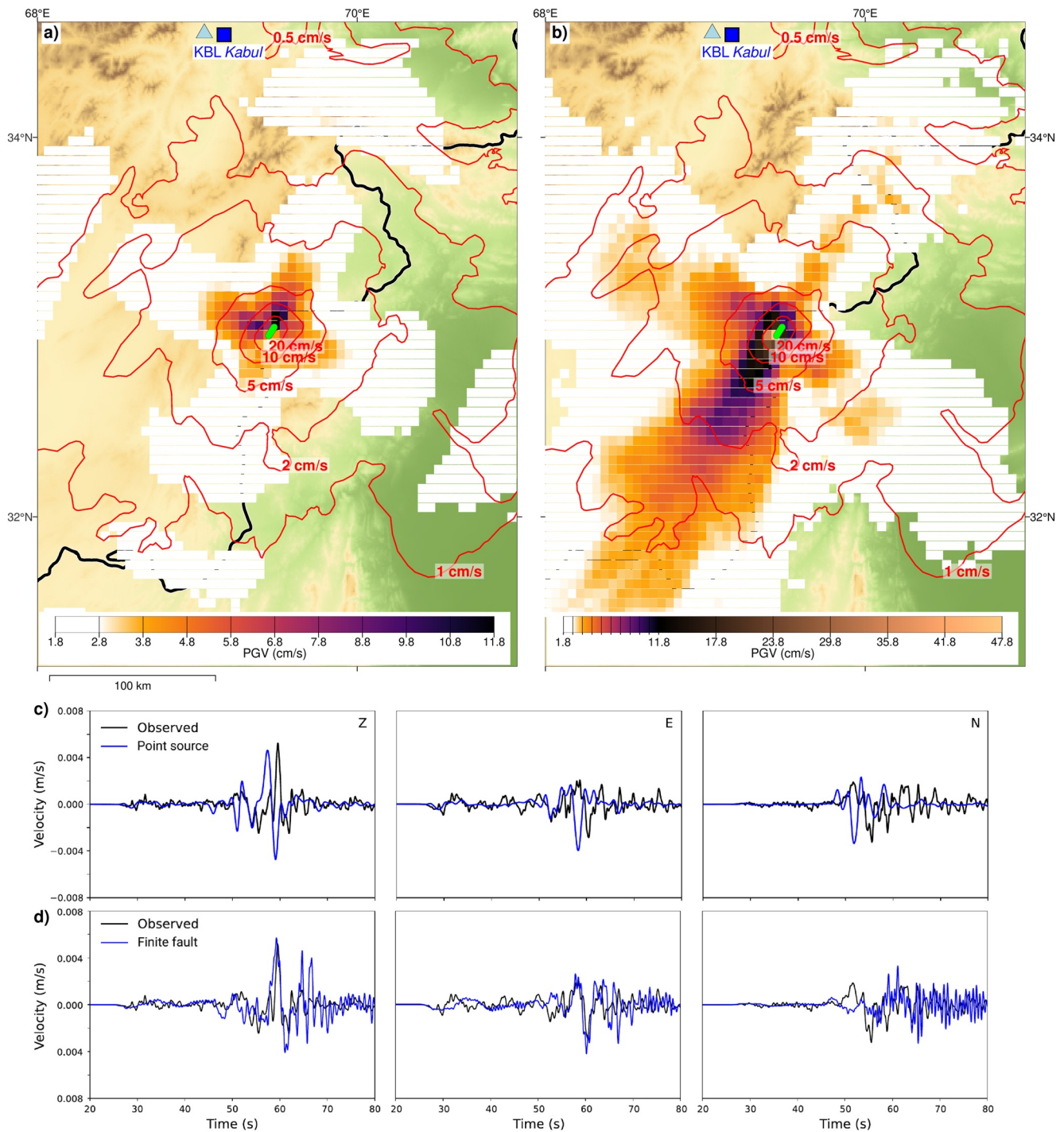
Figure 4. Peak-Ground-Velocity (PGV) maps and waveform fits. (a) PGV map for a point-source simulation at 10 km depth compared to the USGS empirical estimation (USGS, 2022a; red contours). (b) PGV map for finite-fault simulations for 4 km depth and 2 km/s rupture velocity. Red curves as in (a). (c) Comparison at station KBL between the synthetic (blue) and observed (black) waveforms for the single-point-source simulation of (a). (d) Waveform comparison for the finite-fault simulation of (b).

contributing to the large death toll. However, additionally, a number of event-specific faulting characteristics added to this: (a) Regarding the large-scale effect of the earthquake, our PGV simulation clearly shows high PGV values to the SW of the sub-vertical fault, and thus high shaking intensity on the Afghan side, where indeed most destruction has been recorded (European Union, 2022). (b) The similarity in the orientations of the rock foliation

and the earthquake strike may have promoted surface ruptures despites the moderate size of the earthquake. Laboratory experiments demonstrate that shear failure occurs at the lowest shear stress if rock foliation and shear direction are closest (Ikari et al., 2015), which was the case for the Afghanistan earthquake. This consistency may have resulted in more severe destruction in the close vicinity to the fault compared to similar other events globally. (c) Lastly, we speculate that the large maximum slip of the Afghanistan event together with the one-story buildings, typical for the Afghan-Pakistan border region, could have had an impact on the destruction. In the near-field, the constructive effect of rupture directivity and large slip may result in large ground shaking (sometimes referred to as "killer pulse") around 1 Hz frequency (Heaton et al., 1995; Shimizu, 2011). This frequency, in turn, corresponds to the response frequency of one-story buildings (Arnold, 2006). Moreover, the amplitude of the pulse is comparable to that of the fault slip (Heaton et al., 1995), which was unusually large for the Afghanistan event.

In general it is notable that the Mw6.2 Afghanistan earthquake had a huge impact although the magnitude was moderate. Magnitude 6 events are not rare; for example, USGS (2022b) lists ∼140 M6 events per year on average over the last 20 years. The sinistral strike-slip faulting of the Afghanistan earthquake is not surprising either, as it is typical for the regional tectonic setting. The event occurred in an area of increased seismic hazard as indicated by a recent probabilistic seismic hazard assessment (Waseem et al., 2019). However, the increased seismic hazard was solely attributed to thrusting events along the plate boundary fault. Instead, the earthquake ruptured a secondary, shallow, and partly unmapped fault in a region of diffuse deformation - features often found in regions of continental collision and partitioned deformation. Earthquakes of similar size may hit at any location in such deformation belts, emphasizing the need for better preparedness and also taking regions of diffuse deformation into account in modern seismic hazard assessment as associated earthquakes are often shallow and therefore driving the hazard. Detailed small-scale (seismo-)tectonic studies focusing on the 3D shallow crustal structure may help to identify such areas of enhanced seismic hazard. Our study shows that by combining modern remote sensing techniques, persistent search for seismological data sets, and incorporating 3D waveform modeling, it is possible to determine detailed source parameters for M6 earthquakes in remote and inaccessible regions complementing our current understanding of earthquake processes.

Data Availability Statement

All data needed to evaluate the conclusions in the paper are provided in the paper and/or the Supporting Information S1. Raw data and text files to reproduce figures are provided in an open research depository under the https://doi.org/10.5445/IR/1000153077. The waveform data for the KR, IU, and II networks were downloaded from the IRIS data management center. Using the BREQ_FAST interface (http://ds.iris.edu/ds/nodes/dmc/forms/breqfast-request/) and the station names and processing time windows specified in the manuscript, waveform data can be downloaded from this website. Data for the PK, IR, and IM networks were provided through the Meteorological Survey of Pakistan (website: https://www.pmd.gov.pk/en/; FDSN network code: https://www.fdsn.org/networks/detail/PK/; no DOI attached), the Iranian Seismological Center (IRSC; website: https://geophysics.ut.ac.ir/en/; FDSN network code: https://www.fdsn.org/networks/detail/I2/; no DOI attached), and the USGS (website: https://www.usgs.gov/; FDSN network code: https://www.fdsn.org/networks/detail/IM/; no DOI attached), respectively. Please note that these are only the general webpages of the agencies that provided the data as the data is publicly not available online. Therefore the raw waveform data that had been used in this study can be found via the above mentioned DOI. Sentinel 1A SAR data are from ESA/Copernicus (https://scihub.copernicus.eu). Here also only the general landing page is given as processed interferograms are available from our online depository. The free software GMT (https://www.generic-mapping-tools.org/) and python/obspy (https://docs.obspy.org/) were used in this study. Salvus (https://mondaic.com/docs/) was used for PGV calculations. The KIT in-house AmΦB - "Amphibious Bayesian" software (Lindner et al., 2022) was used for RMT inversion. The code is available via https://github.com/seismoMSL/AmPHIB. SAR interferograms and coherence maps were generated with the open source package GMTSAR (Sandwell et al., 2011). The raw data (InSAR, seismic waveforms) used for analysis and results (slip model, PGV) is available via the KIT open repository (https://dbkit.bibliothek.kit.edu/catalog) under the https://doi.org/10.5445/IR/1000153077.

References

Afanasiev, M., Boehm, C., van Driel, M., Krischer, L., Rietmann, M., May, D. A., et al. (2019). Modular and flexible spectral-element waveform modelling in two and three dimensions. *Geophysical Journal International*, *216*(3), 1675–1692. https://doi.org/10.1093/gji/ggy469

Ambraseys, N., & Bilham, R. (2011). Corruption kills. *Nature*, *469*(7329), 153–155. https://doi.org/10.1038/469153a

Arnold, C. (2006). Earthquake effects on buildings 4. *Earthquakes A Man. Archit. Fema* (p. 454).

Avouac, J. P., Ayoub, F., Leprince, S., Konca, O., & Helmberger, D. V. (2006). The 2005, Mw 7.6 Kashmir earthquake: Sub-pixel correlation of ASTER images and seismic waveforms analysis. *Earth and Planetary Science Letters*, *249*(3–4), 514–528. https://doi.org/10.1016/j.epsl.2006.06.025

Bagnardi, M., & Hooper, A. (2018). Inversion of surface deformation data for rapid estimates of source parameters and uncertainties: A Bayesian approach. *Geochemistry, Geophysics, Geosystems*, *19*(7), 2194–2211. https://doi.org/10.1029/2018GC007585

Bayik, C. (2021). Deformation analysis of 2020 Mw 5.7 Karlıova, Turkey, earthquake using DInSAR method with different incidence angle SAR data. *Arabian Journal of Geosciences*, *14*(4), 1–12. https://doi.org/10.1007/s12517-021-06670-x

Bernard, M., Shen-Tu, B., Holt, W. E., & Davis, D. M. (2000). Kinematics of active deformation in the Sulaiman Lobe and Range, Pakistan. *Journal of Geophysical Research*, *105*(B6), 13253–13279. https://doi.org/10.1029/1999jb900405

Bie, L., Ryder, I., Nippress, S. E., & Bürgmann, R. (2014). Coseismic and post-seismic activity associated with the 2008 Mw 6.3 Damxung earthquake, Tibet, constrained by InSAR. *Geophysical Journal International*, *196*(2), 788–803. https://doi.org/10.1093/gji/ggt444

Bommer, J. J., & Alarcon, J. E. (2006). The prediction and use of peak ground velocity. *Journal of Earthquake Engineering*, *10*(1), 1–31. https://doi.org/10.1080/13632460609350586

Brengman, C. M., Barnhart, W. D., Mankin, E. H., & Miller, C. N. (2019). Earthquake-scaling relationships from geodetically derived slip distributions. *Bulletin of the Seismological Society of America*, *109*(5), 1701–1715. https://doi.org/10.1785/0120190048

Copernicus. (2022). Emergency Management Service - Mapping. Retrieved from https://emergency.copernicus.eu/mapping/list-of-components/EMSR584/

DeMets, C., Gordon, R. G., & Argus, D. F. (2010). Geologically current plate motions. *Geophysical Journal International*, *181*(1), 1–80. https://doi.org/10.1111/j.1365-246x.2009.04491.x

Dziewonski, A. M., Chou, T. A., & Woodhouse, J. H. (1981). Determination of earthquake source parameters from waveform data for studies of global and regional seismicity. *Journal of Geophysical Research*, *86*(B4), 2825–2852. https://doi.org/10.1029/jb086ib04p02825

Ekström, G., Nettles, M., & Dziewoński, A. M. (2012). The global CMT project 2004–2010: Centroid-moment tensors for 13,017 earthquakes. *Physics of the Earth and Planetary Interiors*, *200*, 1–9. https://doi.org/10.1016/j.pepi.2012.04.002

European Union. (2022). Map produced by the JRC. Retrieved from https://erccportal.jrc.ec.europa.eu/ECHO-Products/Maps#/maps/4116

Fathian, A., Atzori, S., Nazari, H., Reicherter, K., Salvi, S., Svigkas, N., et al. (2021). Complex co-and postseismic faulting of the 2017–2018 seismic sequence in western Iran revealed by InSAR and seismic data. *Remote Sensing of Environment*, *253*, 112224. https://doi.org/10.1016/j.rse.2020.112224

Gao, Y., Tilmann, F., Yuan, X., Schurr, B., Rietbrock, A., Fichtner, A., et al. (2022). Seismic structure in the crust and upper mantle beneath the Hindu Kush and Pamir from Full Waveform Inversion (No. EGU22-11377). In *Copernicus Meetings*.

Gaudreau, É., Nissen, E. K., Bergman, E. A., Benz, H. M., Tan, F., & Karasözen, E. (2019). The August 2018 Kaktovik earthquakes: Active tectonics in northeastern Alaska revealed with InSAR and seismology. *Geophysical Research Letters*, *46*(24), 14412–14420. https://doi.org/10.1029/2019gl085651

GCMT - Global Centroid Moment Tensor Catalog. (2022). Retrieved from https://www.globalcmt.org/cgi-bin/globalcmt-cgi-bin/CMT5/form?itype=ymd&yr=2022&mo=6&day=21&otype=ymd&oyr=2022&omo=6&oday=21&jyr=1976&jday=1&ojyr=1976&ojday=1&nday=1&lmw=5.7&umw=6.3&lms=0&ums=10&lmb=0&umb=10&llat=30&ulat=35&llon=65&ulon=75&lhd=0&uhd=1000&lts=-9999&uts=9999&lpe1=0&upe1=90&lpe2=0&upe2=90&list=0

Geofon. (2022). *Earthquake Bulletins*. On-Line Bulletin by the German Research Centre for Geosciences. Retrieved from https://geofon.gfz-potsdam.de/old/eqinfo/event.php?id=gfz2022mcak

Google Earth Pro V7.3.4.8248. (2022). Afghan-Pakistan border region (approx. 33N, 069.4E). Eye alt. 46 km, 4 km, and 0.5 km. Image 2022 Maxar Technologies and 2022 CNES/Airbus. Image date: 6.9.2021. Retrieved from http://www.earth.google.com

Heaton, T. H., Hall, J. F., Wald, D. J., & Halling, M. W. (1995). Response of high-rise and base-isolated buildings to a hypothetical Mw 7.0 blind thrust earthquake. *Science*, *267*(5195), 206–211. https://doi.org/10.1126/science.267.5195.206

Hirt, C., & Rexer, M. (2015). Earth2014: 1 arc-min shape, topography, bedrock and 112 ice-sheet models – Available as gridded data and degree-10,800 spherical harmonics. *International Journal of Applied Earth Observation and Geoinformation*, *39*, 103–112. https://doi.org/10.1016/j.jag.2015.03.001

Ikari, M. J., Niemeijer, A. R., & Marone, C. (2015). Experimental investigation of incipient shear failure in foliated rock. *Journal of Structural Geology*, *77*, 82–91. https://doi.org/10.1016/j.jsg.2015.05.012

Isik, V., Saber, R., & Caglayan, A. (2021). November 08, 2019 Turkmanchay earthquake (Mw: 5.9) in NW Iran: An assessment of the earthquake using DInSAR time-series and field evidence. *Natural Hazards*, *105*(3), 3013–3037. https://doi.org/10.1007/s11069-020-04439-1

Jiang, G., Wen, Y., Liu, Y., Xu, X., Fang, L., Chen, G., et al. (2015). Joint analysis of the 2014 Kangding, southwest China, earthquake sequence with seismicity relocation and InSAR inversion. *Geophysical Research Letters*, *42*(9), 3273–3281. https://doi.org/10.1002/2015gl063750

Jo, M. J., Jung, H. S., & Yun, S. H. (2017). Retrieving precise three-dimensional deformation on the 2014 M6. 0 South Napa earthquake by joint inversion of multi-sensor SAR. *Scientific Reports*, *7*(1), 1–10. https://doi.org/10.1038/s41598-017-06018-0

Kobayashi, T. (2017). Earthquake rupture properties of the 2016 Kumamoto earthquake foreshocks (M j 6.5 and M j 6.4) revealed by conventional and multiple-aperture InSAR. *Earth, Planets and Space*, *69*(1), 1–12. https://doi.org/10.1186/s40623-016-0594-y

Lindner, M., Rietbrock, A., Bie, L., Goes, S., Collier, J., Rychert, C., et al. (2022). Bayesian regional moment tensor from ocean bottom seismograms recorded in the Lesser Antilles: Implications for regional stress field. Retrieved from https://arxiv.org/abs/2206.05502

Liu, J., Hu, J., Xu, W., Li, Z., Zhu, J., Ding, X., & Zhang, L. (2019). Complete Three-Dimensional Coseismic Deformation Field of the 2016 Central Tottori Earthquake by Integrating Left-and Right-Looking InSAR Observations With the Improved SM-VCE Method. *Journal of Geophysical Research: Solid Earth*, *124*(11), 12099–12115. https://doi.org/10.1029/2018jb017159

Mohadjer, S., Ehlers, T. A., Bendick, R., Stübner, K., & Strube, T. (2016). A Quaternary fault database for central Asia. *Natural Hazards and Earth System Sciences*, *16*(2), 529–542. https://doi.org/10.5194/nhess-16-529-2016

Niu, Y., Wang, S., Zhu, W., Zhang, Q., Lu, Z., Zhao, C., & Qu, W. (2019). The 2014 Mw 6.1 Ludian earthquake: The application of RADARSAT-2 SAR interferometry and GPS for this conjugated ruptured event. *Remote Sensing*, *12*(1), 99. https://doi.org/10.3390/rs12010099

NOAA - National Oceanic and Atmospheric Administration, National Centers for Environmental Information. (2023). Retrieved from https://www.ngdc.noaa.gov/hazel/view/hazards/earthquake/search

Okada, Y. (1985). Surface deformation due to shear and tensile faults in a half-space. *Bulletin of the Seismological Society of America*, *75*(4), 1135–1154. https://doi.org/10.1785/bssa0750041135

Pavlis, N. K., Holmes, S. A., Kenyon, S. C., & Factor, J. K. (2012). The development and 135 evaluation of the Earth Gravitational Model 2008 (EGM2008). *Journal of Geophysical Research: Solid Earth*, *117*(B4). https://doi.org/10.1029/2011JB008916

Penney, C., Copley, A., & Oveisi, B. (2015). Subduction tractions and vertical axis rotations in the Zagros–Makran transition zone, SE Iran: The 2013 May 11 Mw 6.1 Minab earthquake. *Geophysical Journal International*, *202*(2), 1122–1136. https://doi.org/10.1093/gji/ggv202

Ross, Z. E., Kanamori, H., Hauksson, E., & Aso, N. (2018). Dissipative intraplate faulting during the 2016 Mw 6.2 Tottori, Japan earthquake. *Journal of Geophysical Research: Solid Earth*, *123*(2), 1631–1642. https://doi.org/10.1002/2017jb015077

Ruleman, C. A., Crone, A. J., Machette, M. N., Haller, K. M., & Rukstales, K. S. (2007). Map and database of probable and possible Quaternary faults in Afghanistan. *US Geological Survey Open-File Report*, *1103*(1).

Sandwell, D. T., Mellors, R., Xiaopeng, T., Wei, M., & Wessel, P. (2011). Open radar interferometry software for mapping surface deformation. *Eos, Transactions American Geophysical Union*, *92*(28), 234–235. https://doi.org/10.1029/2011EO280002

Shearer, P. (2009). *Introduction to seismology* (2nd ed.). Cambridge University Press.

Shimizu, S. (2011). Behaviour of steel columns under 3-D seismic load. *Thin-Walled Structures*, *49*(5), 544–553. https://doi.org/10.1016/j.tws.2010.09.016

Simmons, N. A., Myers, S. C., Morency, C., Chiang, A., & Knapp, D. R. (2021). SPiRaL: A multiresolution global tomography model of seismic wave speeds and radial anisotropy variations in the crust and mantle. *Geophysical Journal International*, *227*(2), 1366–1391. https://doi.org/10.1093/gji/ggab277

Tape, W., & Tape, C. (2016). A confidence parameter for seismic moment tensors. *Geophysical Journal International*, *205*(2), 938–953. https://doi.org/10.1093/gji/ggw057

USGS - United States geological Survey. (2022a). Retrieved from https://earthquake.usgs.gov/earthquakes/eventpage/us7000hj3u

USGS - United States geological Survey. (2022b). Retrieved from https://earthquake.usgs.gov/earthquakes/search/

Wald, D. J., & Allen, T. I. (2007). Topographic slope as a proxy for seismic site conditions and amplification. *Bulletin of the Seismological Society of America*, *97*(5), 1379–1395. https://doi.org/10.1785/0120060267

Waseem, M., Lateef, A., Ahmad, I., Khan, S., & Ahmed, W. (2019). Seismic hazard assessment of Afghanistan. *Journal of Seismology*, *23*(2), 217–242. https://doi.org/10.1007/s10950-018-9802-5

Worden, C. B., Gerstenberger, M. C., Rhoades, D. A., & Wald, D. J. (2012). Probabilistic relationships between ground-motion parameters and modified Mercalli intensity in California. *Bulletin of the Seismological Society of America*, *102*(1), 204–221. https://doi.org/10.1785/0120110156

World Meteorological Organization. (2022). Retrieved from https://public.wmo.int/en/media/news/normal-above-normal-rainfall-forecast-southwest-monsoon

Yun, S. H., Hudnut, K., Owen, S., Webb, F., Simons, M., Sacco, P., et al. (2015). Rapid damage mapping for the 2015 Mw 7.8 Gorkha earthquake using synthetic aperture radar data from COSMO–SkyMed and ALOS-2 satellites. *Seismological Research Letters*, *86*(6), 1549–1556. https://doi.org/10.1785/0220150152

Erratum

In the originally published version of this article, author L. Bie was omitted from the Author Contributions in the categories of conceptualization, data curation, formal analysis, investigation, methodology, project administration, resources, software, validation, visualization, writing – original draft, and writing – review and editing. The Author Contributions have been corrected, and this may be considered the authoritative version of record.